

Tailoring the Salt Concentration in a Gel-Solid Polymer Electrolyte to Stabilize High-Voltage LiCoMnO₄ Cathode

Sreekumar Sreedeeep, Yun-Sung Lee,* and Vanchiappan Aravindan*

Here, an attempt is made to depict the role of salt concentration on the electrochemical stability of a gel interface formed by the in-situ polymerization of a commercial liquid electrolyte on solid-polymer support, which is the so-called gel-solid polymer electrolyte (G-SPE). The electrochemical characterization of the electrolyte exhibits high ionic conductivity in the order of $\approx 10^{-3} \text{ S cm}^{-1}$ at ambient temperature, while the same increases as the LiPF₆ concentration varies from 1 to 3 M. Further, the flammability test has shown the flame-retardant nature of the G-SPE compared to the liquid electrolyte. The stability of the G-SPE is analyzed in a half-cell configuration with a high-voltage LiCoMnO₄ cathode. Also, anode and anode-less cell configurations with LiCoMnO₄ cathode against Li₄Ti₅O₁₂ and Cu are carried out with G-SPE-2 M as the electrolyte. In addition, post-mortem analysis, like XRD, XPS, EDS, SEM, etc., of the cycled LiCoMnO₄ electrode and G-SPE is carried out to understand the occurrence of any material degradation or electrolyte decomposition during cycling.

a significant breakthrough in battery technology, revolutionizing the modern world.^[7–10] The innumerable applications of LIBs range from their usage in small-scale portable electronic devices such as mobile phones and laptops to large-scale electric vehicles (EVs) and grid storage applications. In addition, with the surge in the demand for EVs, there has been a tremendous increase in the research and development of LIBs.^[9,11]

However, various parameters associated with LIBs have yet to be improved, of which improving their energy density acquires prime importance. As energy is proportional to the operating potential and specific capacity of the respective electrodes, the optimization of the active material is required to produce high-energy-density LIBs.^[12–16] The state-of-the-art LIBs rely upon conventional cathodes such as LiCoO₂^[17–19]

and LiNi_xMn_yCo_zO₂,^[20–22] with graphite as the anode, which encounters the issue of poor energy density, hence motivating the search for alternate electrode materials. Revisiting Li-metal batteries (LMB) with high volumetric and gravimetric capacities, high energy density, and low reduction potential (−3.04 V vs. Li) is worth mentioning. However, the large-scale commercialization of LMBs has not yet been achieved due to the limited improvement in electrolytes and non-uniform dendritic growth, causing safety issues, poor coulombic efficiency, and fast capacity fading. Moreover, the low electrochemical stability window of the conventional liquid electrolytes ($\approx 4.3 \text{ V}$ vs. Li, for carbonate electrolyte) will hamper high energy and power requirements. Therefore, there requirement of an alternative electrolyte system with better electrochemical stability and cell safety is essential for the development of LIBs. This eventually led to the development of next-generation electrolytes called solid-state electrolytes (SSE).^[23]

The SSEs possess several desirable features of an ideal electrolyte system, which include excellent electrochemical stability window, good thermal stability, and good ionic conductivity comparable to the liquid electrolyte ($\approx 10^{-2}$ – $10^{-3} \text{ S cm}^{-1}$). In addition, its ability to mitigate the irregular Li⁰ deposition mitigates the issue of dendritic formation, hence improving cell safety. However, several setbacks with SSEs have to be addressed, prominent among them are the poor electrode-electrolyte contact causing high interfacial resistance. Although strategies such as high temperature and pressure sintering are promising, employing them for the development of LMBs on an economical and commercial scale is less feasible.

1. Introduction

The rapid rise in global warming and climate change has hampered the growth of the modern world. Although fossil fuels are considered the primary energy source, the over-exploitation of these resources has led to their depletion from the earth's crust. Moreover, the combustion of fossil fuels evolving greenhouse gases contributes a major share of global warming.^[1–3] Although renewable energy, due to its sustainability and environmental benignity, is considered an alternative to fossil fuels, its transient and inconsistent nature adversely affects its implementation.^[4–6] Hence, the storage of this energy is a primary concern, and this has led to the development of energy storage devices. Prominent among them are electrochemical energy storage devices such as batteries. The advancement in Li-ion batteries (LIBs) has created

S. Sreedeeep, V. Aravindan
Department of Chemistry
Indian Institute of Science Education and Research (IISER)
Tirupati, Andhra Pradesh 517619, India
E-mail: aravindan@iisertirupati.ac.in

Y.-S. Lee
School of Chemical Engineering
Chonnam National University
Gwang-ju 61186, Republic of Korea
E-mail: leeys@chonnam.ac.kr

The ORCID identification number(s) for the author(s) of this article can be found under <https://doi.org/10.1002/sml.202503594>

DOI: 10.1002/sml.202503594

Polymer-based solid electrolytes, also called solid-polymer electrolytes (SPEs), are a better substitute for SSEs. In SPEs, the Li-salts are dissolved in a polymer matrix such as Poly(ethylene oxide) (PEO), Poly(vinylidene fluoride-co-hexafluoropropylene) (PVdF-HFP), Poly(acrylonitrile) (PAN) forming a “salt-in-polymer” based system.^[24,25] The SPEs exhibit an improved Li-ion conduction compared to the SSEs and are more flexible. In addition, compared to SSEs such as $\text{Li}_{10}\text{GeP}_2\text{S}_{12}$, which is moisture sensitive and forms insulating byproducts.^[26,27] However, similar to SSEs, the SPEs also render poor electrode-electrolyte contact and interfacial resistance. Strategies like adding 2D/3D fillers (BN, SiO_2) or forming a cross-linking framework within the electrolyte enhance the Li-ion conduction mechanical, and thermal stabilities. However, such a strategy is not effective in mitigating the interfacial contact issues.^[26] The formation of an interlayer so-called gel between the electrode and the electrolyte is an effective and promising approach to mitigate the contact issue. In this method, an in-situ polymerization will be carried out in which the monomer or the polymerizable molecules are easily polymerized by an initiator in the presence of heat or light. The as-formed gel will improve the contact between the electrode and electrolyte. In addition, it also facilitates the Li-ion transfer within the electrode and electrolyte.^[28]

In this work, we attempt to improve electrolyte contact by forming an interfacial gel between the electrode and electrolyte. A polymeric film has been made with PVdF-HFP polymer and boron nitride (BN) as filler. In the SPE film, the BN plays a crucial role in enhancing the Li-ion conduction by providing additional channels. Further, the high thermal stability of the BN ($\approx 1000^\circ\text{C}$) will enhance the thermal stability of the polymeric film. The electrochemical contact between the as-prepared film and the electrode has been improved by the in-situ polymerization of liquid electrolyte into a gel by a thermal initiation using an initiator. In addition, the influence of the electrolyte salt concentration on the stability of the gel has been analyzed by varying the LiPF_6 concentration. Further, the high voltage stability of the G-SPE has been analyzed in a half-cell configuration with LiCoMnO_4 as the cathode. The LiCoMnO_4 has a spinel structure with a theoretical capacity of 145 mAh g^{-1} and an operating potential of 5V (vs. Li). The high operating potential of LiCoMnO_4 will enhance the energy density, hence making it suitable for high-energy-density LIBs. However, poor cycle stability of LiCoMnO_4 due to electrolyte decomposition at high operating potential is a serious setback that has to be addressed.^[29–32] Here, we use the G-SPE: 1–3 M electrolytes to enhance the stability and improve the rate capability of LiCoMnO_4 . Apart from half-cell, the stability of the G-SPE has been depicted in both full- and anode-less cell configurations with LiCoMnO_4 as cathode and $\text{Li}_4\text{Ti}_5\text{O}_{12}$ and Cu as the respective counter electrodes for full- and anode-less cells.

2. Results and Discussion

2.1. Physical and Material Characterization of G-SPE

The structural feature of the G-SPE was determined by the XRD analysis, as shown in Figure 1a. The diffraction peaks corresponding to the crystal plane (100) and (020) indicate the PVdF-HFP polymer matrix in the film, whereas the sharp, intense peak corresponding to the (002) crystal plane denotes the BN filler in

the matrix. The XRD spectra of the pristine LCMO (Figure 1b) depict characteristic peaks corresponding to crystal planes (111), (311), (444), and (440), hence showing the formation of LCMO by a co-precipitation synthesis method. The IR spectral analysis (Figure 1c) has been carried out for both G-SPE:1 M and G-SPE:3 M to understand the functional groups present in the electrolyte. The peaks corresponding to 714 , 774 , and 964 cm^{-1} correspond to the rocking, wagging, and bending vibrational modes of the C–H bond in the $-\text{CH}_2$ group of the PVdF-HFP polymer matrix (Figure 1c). Also, the intense vibrational band at 1067 cm^{-1} corresponds to the C–F functionality of the $-\text{CF}_3$ moiety in the polymeric matrix. In addition, the highly intense band at 1773 and 1804 cm^{-1} corresponds to the C=O functionality of the EC and DMC in the gel part of the electrolyte. Moreover, the intense peak positioned at 843 cm^{-1} corresponds to the free PF_6^- group in the electrolyte, while the less intense peak at 834 cm^{-1} further signifies that only a small portion of PF_6^- is in coordination with the Li-ions. Hence, a complete dissociation of LiPF_6 in the electrolyte was revealed. In addition, vibrational bands at 1274 , 1391 , 1457 , and 1483 cm^{-1} correspond to the symmetric and asymmetric vibrational modes of C–O, C–H, and C=O functionalities in EC and DMC. Also, both G-SPE:1 M and G-SPE:3 M electrolytes exhibit similar kinds of peaks, while the peak intensity of G-SPE:3 M is lower compared to the G-SPE:1 M. The $^1\text{H-NMR}$ spectra (Figures S1 and S2, Supporting Information) of the polymerized gel-electrolyte illustrate the formation of Polyethylene carbonate (PEC), which is formed by the ring-opening polymerization of EC by AIBN. The $^1\text{H-NMR}$ spectra of G-SPE: 2 M show an intense peak corresponding to the H_b proton ($\approx 3.8\text{ ppm}$) of the polymerized PEC, while the H_g ($\approx 4.9\text{ ppm}$) proton corresponds to the unpolymerized EC in the polymer electrolytes. Therefore, the $^1\text{H-NMR}$ analysis successfully illustrates the ring-opening polymerization of EC into PEC in neutral media, and this conversion is the crucial step for the in-situ transformation of the liquid electrolyte into a gel electrolyte.

The structural and morphological aspects of the polymeric film and the LCMO were analyzed using FE-SEM. The FE-SEM images of LCMO depict its unique spherical morphology, which is similar to single-crystalline cathode materials. The cross-sectional FE-SEM (Figure S3, Supporting Information) images of the as-prepared PVdF-HFP-BN polymeric film show its porous nature, which is anticipated to enhance the infiltration of liquid electrolytes into the film. The amount of liquid electrolyte infiltrated into the film has been quantified using Equation (4) to be 80, 70, and 50% for the 1, 2, and 3 M electrolytes. This trend in the liquid electrolyte infiltration into the polymeric film can be attributed to the increase in the viscosity of the liquid electrolytes as the electrolyte concentration is increased from 1 to 3 M. The TGA analysis (Figure 1d) exhibits a weight loss of 47.39 and 53.65% among the G-SPE-1 and 3 M electrolytes. In addition, the pore radius and surface area of the polymeric film are quantified from the BET analysis to be $\approx 14.7\text{ \AA}$ and $\approx 62.9\text{ m}^2\text{ g}^{-1}$ (Figure 1e). Also, the pore size distribution plot of the polymeric film is shown in Figure 1f. The stress-strain analysis of the G-CPE has been shown in Figure S4 (Supporting Information), wherein the G-SPE: 3 M exhibits a high yield strength of 7 MPa while the G-SPE: 1 M shows a comparatively low yield strength of 4 MPa. In addition, the G-SPE: 3 M shows high flexibility compared to the G-SPE: 1 M, which is evident from the stress-strain

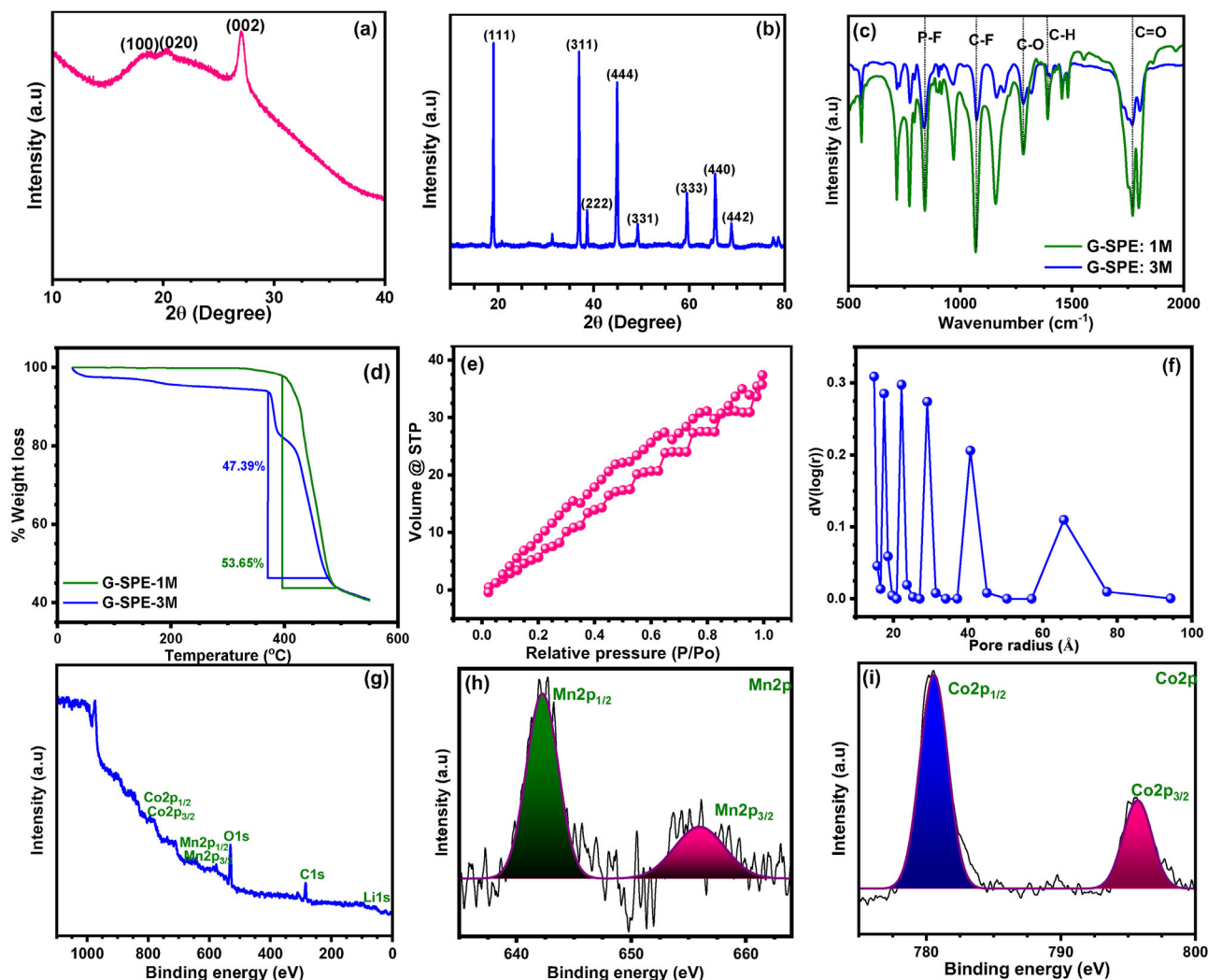


Figure 1. a,b) XRD of G-SPE: 1 M and LCMO, and c) IR spectral analysis of G-SPE:1 M, and G-SPE:3 M, electrolytes, d) TGA analysis of G-SPE-1 and 3 M, e,f) BET analysis of the polymeric film, g-i) XPS analysis of LCMO.

curve. The XPS spectral analysis of LCMO shows the surface elemental composition of Li, Co, Mn, O, and C in the compound (Figure 1g–i). Further, the transition metal peaks corresponding to Co and Mn reveal their oxidation state to be + 3 and + 4, respectively.

The flammability test of the G-SPEs has been carried out to monitor the safety of the electrolyte. As shown in Figure 2, the flammability test begins with igniting the electrolytes and monitoring them for a certain duration (here, 15 s). As assumed, the liquid electrolytes caught fire easily, and the flame was sustained until the electrolyte was completely burned out. However, the G-SPEs do not catch fire and resist the flame for the measured 15 s compared to liquid electrolytes.

2.2. Theoretical Perspective of the G-SPE

The interaction of the Li-ions with the electrolyte has been quantified by the neighboring bond orbital (NBO) calculations.

Table S1 (Supporting Information) shows that the interactions between the Li-ions with EC and DMC will be considered as the core-shell electrons (CR) of Li-ion and the σ^* , π^* orbitals of DMC and EC. The interaction between the DMC and Li-ion is from the CR of the Li-ions to the σ^* -orbital of the C–O and C–H bond in the DMC molecule, while in the case of EC and Li-ion, the interaction occurs between the σ^* and π^* orbitals of C–O and C–H bond in the EC molecule and the CR of the Li-ion. In addition, the delocalization energy (E_2), which indicates the stability of the interaction, shows a higher magnitude of E_2 for the interaction between DMC and Li-ion compared to EC and Li-ion. This increase in the magnitude of E_2 for the interaction between DMC and Li-ions suggests that the DMC molecules are bound to the Li-ions, while the low magnitude of E_2 for the interaction between EC and Li-ions shows that EC molecules are free, which further indicates that the EC molecules facilitate the gel formation compared to DMC. Improving the electrolyte stability window is necessary to prevent electrolyte decomposition at high operating potentials. Here, DMC and EC are the main constituents

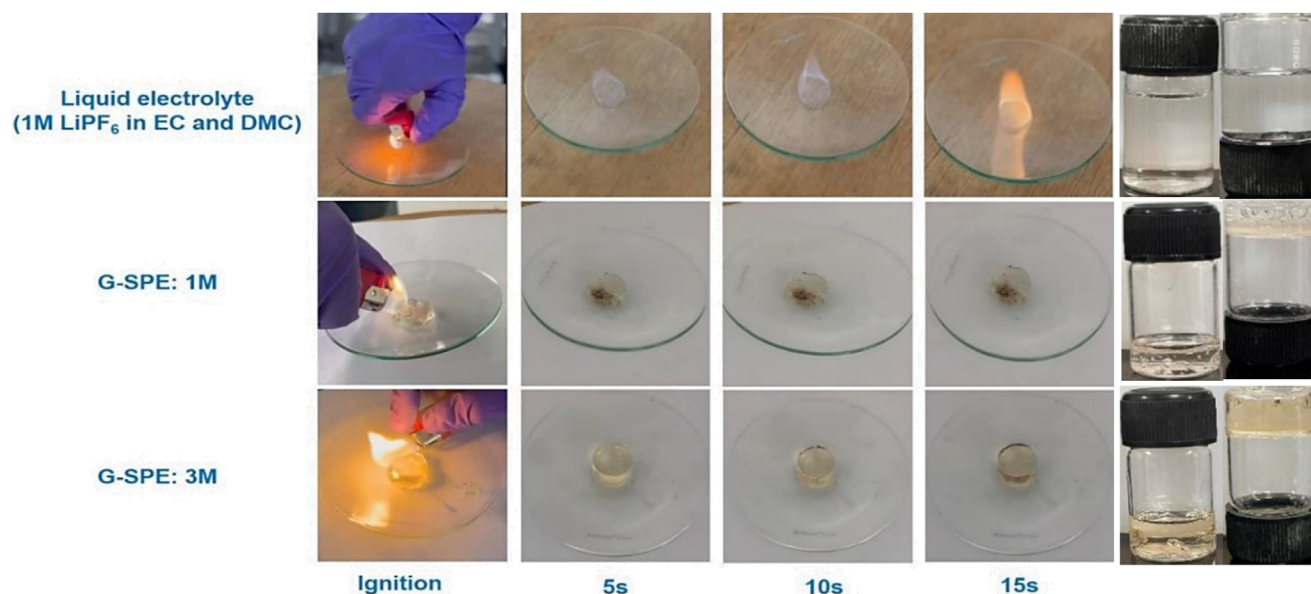


Figure 2. Flammability test of liquid, G-SPE:1 M, and G-SPE:3 M electrolytes at different durations of 5, 10, and 15 s.

of the liquid electrolyte. Therefore, it is necessary to determine the HOMO-LUMO energy gap of both these constituents to understand the stability of the electrolyte. From Figures S5 and S6 (Supporting Information), the energy of HOMO and LUMO for the DMC are -9.8 and -1.9 eV with a ΔE value of 7.9 eV, while for EC, it is -1.6 and -7.9 eV with a ΔE value of 6.3 eV. Hence, the gel formed by combining both these components will have an ΔE value much higher compared to the individual constituents, thereby improving the stability of the G-SPE at higher potentials.

2.3. Electrochemical Characterization of the G-SPEs

The Li-ion conduction through the G-SPE has been evaluated from the electrochemical impedance spectroscopy (EIS) analysis of the electrolyte for the symmetric cell configuration SS/G-SPE:1-3 M/SS using the equation given as,

$$\sigma = L/R_b A \quad (1)$$

where L is the thickness of the electrolyte, R_b is the bulk resistance, and A is the contact area of the electrode with the electrolyte. The as-determined magnitudes of the ionic conductivities are in the order of $\approx 10^{-3}$ S cm^{-1} . Also, the magnitudes of the ionic conductivities have been evaluated to be 8.5 , 7.7 , and 6.1 mS cm^{-1} for G-SPE-1 M, G-SPE-2 M, and G-SPE-3 M, respectively. This decrease in the magnitude of the Li-ion conductivity can be attributed to the hindrance to the Li-ion mobility due to the increased viscosity of the electrolyte as the concentration of the LiPF_6 is increased from 1 to 3 M.

The transference number (t_{Li^+}) (Figure 3d–f) has been evaluated from the symmetric cell configuration, Li/G-SPE:1-3 M/Li. The determination of t_{Li^+} has been carried out by combining the

frequency-dependent EIS with the DC polarisation by chronoamperometry using the Bruce–Vincent equation given as

$$t_{\text{Li}^+} = I^{\text{ss}} (\Delta V - I^0 R_i^0) / I^0 (\Delta V - I^{\text{ss}} R_i^f) \quad (2)$$

where I^0 and I^{ss} denote the initial and steady-state current, R_i^0 and R_i^f are the initial and final resistance obtained from EIS, and ΔV is the voltage polarization (10 mV). The magnitudes of t_{Li^+} have been determined to be 0.83 , 0.79 , and 0.75 for G-SPE-1 M, G-SPE-2 M, and G-SPE-3 M, respectively. The decrease in the as-determined magnitudes of t_{Li^+} as the concentration is increased from 1 to 3 M can be attributed to the increase in the bound Li-ions with the solvents, which, when phase-changed into a gel, will decrease the number of mobile Li-ions, thereby decreasing the t_{Li^+} .³³ Table S2 (Supporting Information) shows a comparison of the transference number and ionic conductivity of Li^+ of the previously reported work with this work.

The electrochemical stability of the G-SPEs is an important parameter associated with the stable working of the battery. During galvanostatic charge–discharge (GCD) cycling, there will be a constant stripping/plating of Li-ions on the Li-metal anode. However, non-uniform stripping/plating of the Li-ions will lead to dendrite formation, which eventually damages the electrolyte and short-circuits the cell.³ Therefore, to evaluate the stability of the G-SPEs, the stripping/plating study has been carried out with a symmetric cell configuration of Li/G-SPE:1-3 M/Li at an arial current density of 0.1 mA cm^{-1} as shown in Figure 3a–c. The GSPE:1 M and G-SPE:2 M symmetric cells exhibit stable cycling without polarisation for 2000 and 700 h, respectively. In contrast, G-SPE:3 M exhibits a large polarization during the initial cycling but remains stable as the cycling progresses for 500 h. In addition, LSV analysis (Figure S7, Supporting Information) has been carried out for the electrolytes with a symmetric cell configuration of SS/G-SPE:1-3 M/SS within a potential window ranging up to 7 V vs. Li. From the LSV profile, it can be observed that the

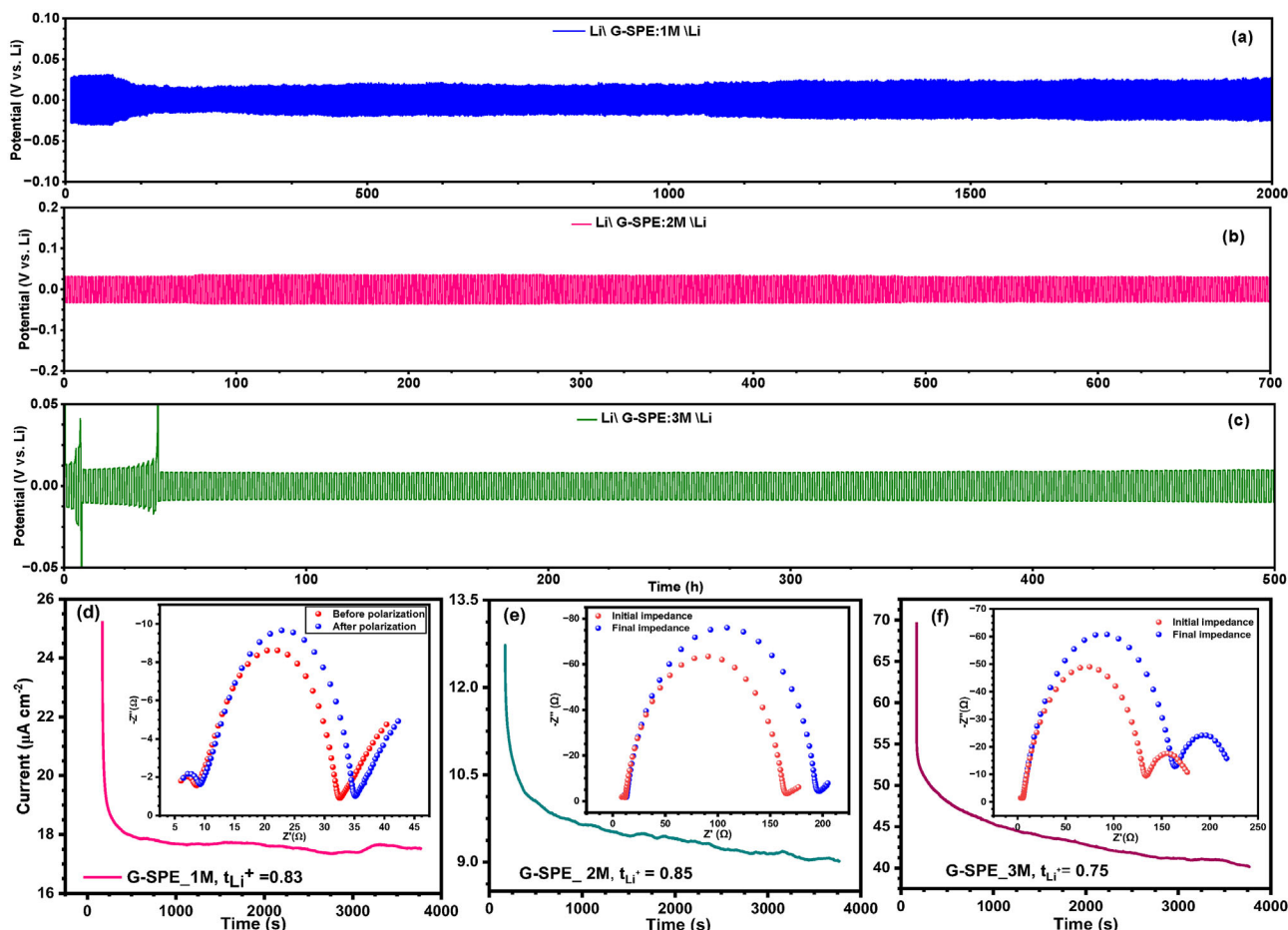


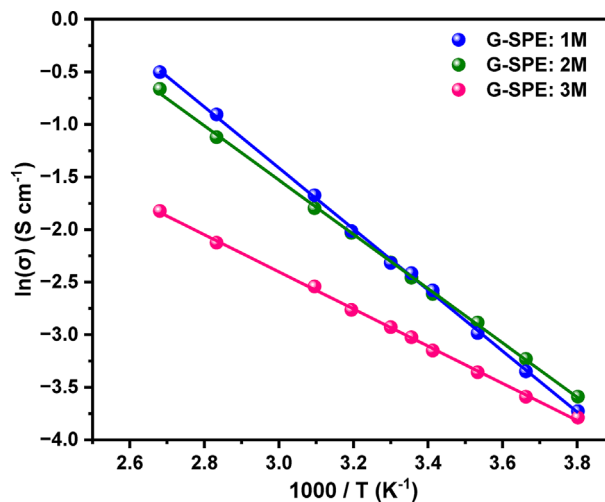
Figure 3. a–c) Stripping-plating analysis, and d–f) transference number calculation for G-SPE:1–3 M from the symmetric cell configuration.

G-SPE:3 M exhibits higher oxidation stability (≈ 6 V vs. Li) followed by G-SPE:2 M (≈ 5 V vs. Li). Conversely, the G-SPE:1 M exhibits poor oxidation stability compared to G-SPE:3 M and G-SPE:2 M, with an oxidation current rise at ≈ 4.6 V vs. Li. This trend in oxidation stability can be explained by the stability and thickness of the LiF-rich insulation coating formed due to the decomposition of LiPF_6 in different electrolytes. For the G-SPE:3 M, quite a large amount of LiF will be formed by the decomposition of LiPF_6 , leading to the formation of a thicker LiF coating. On the other hand, the formation of a small amount of LiF leads to a thinner LiF coating in the case of G-SPE-1 M. Hence, the formation of a thicker LiF protecting layer will enhance the oxidation stability in the case of G-SPE: 3 M compared to G-SPE: 2 M and then G-SPE: 1 M.

The activation energy (E_a) of the electrolyte has been evaluated from the Arrhenius plot (Figure 4) to determine the kinetics of Li-ion through the electrolytes. The activation energy of the electrolyte has been determined from the EIS profile of the electrolytes at different temperatures ranging from -10 to 80 °C using a symmetric cell of the configuration SS/G-SPE/SS. The activation energy has been evaluated from the equation given by

$$\ln(\sigma) = \ln(\sigma_0) - E_a/1000RT$$

where σ is the conductivity of the electrolyte (in S cm^{-1}), E_a is the activation energy, and R is the universal gas constant (8.314 J K^{-1}). The as-determined magnitudes of E_a (Table S3, Supporting Information) are 0.15, 0.25, and 0.32 eV for the G-SPE



(3) Figure 4. Arrhenius plot for the calculation of activation energy.

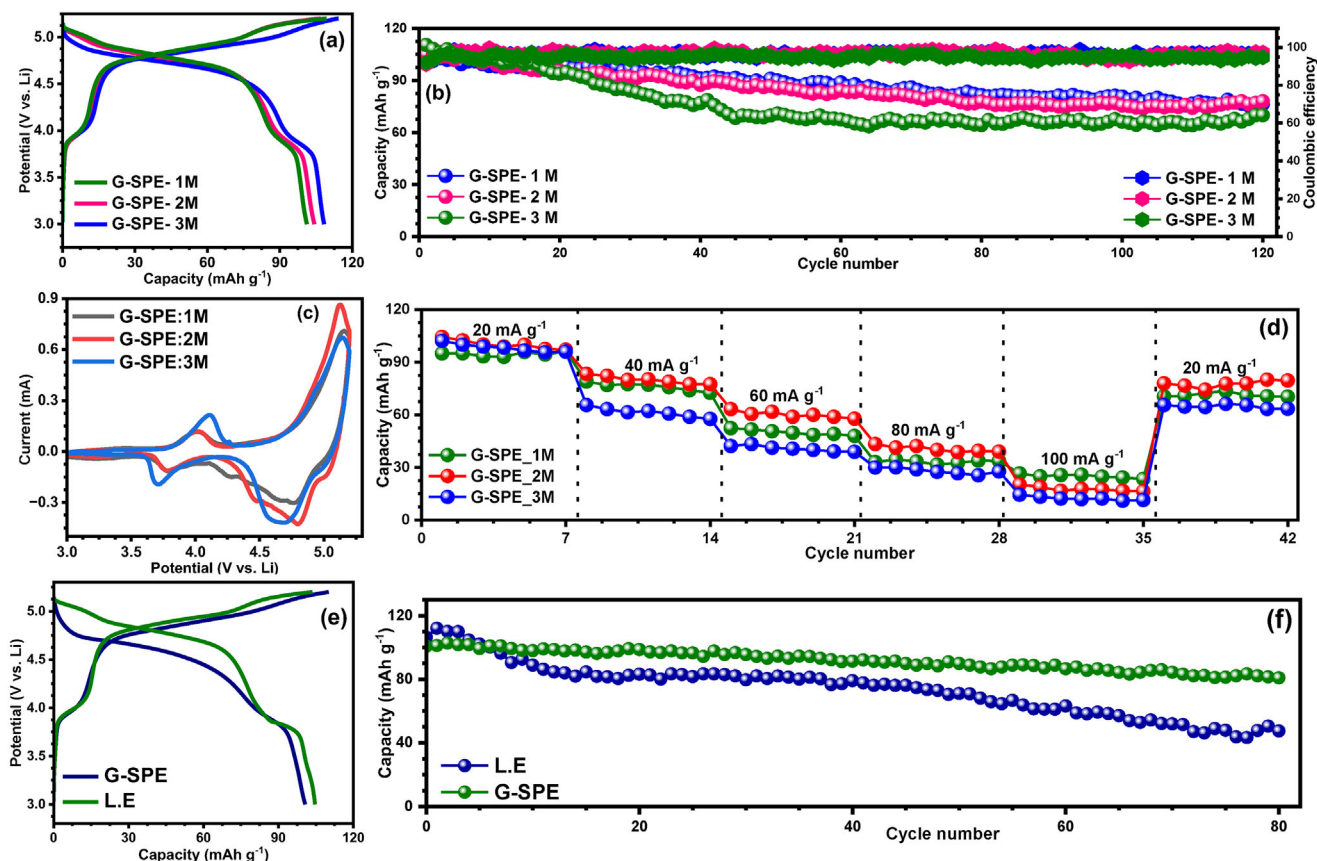


Figure 5. a,b) GCD profiles of LCMO for G-SPE-1–3 M, c) CV profile of G-SPE-1–3 M, d) rate-performance profile of G-SPE-1–3 M, and e,f) GCD profiles of LCMO cycled in G-SPE and liquid electrolyte (L.E.).

concentration of 1, 2, and 3 M. This direct proportionality of E_a with electrolyte concentration can be ascertained due to the strong interaction between the Li-ions and the solvent molecules in the concentrated electrolyte of G-SPE:3 M. However, a decrease in the interaction between the Li-ions and the solvent molecules in the G-SPE-1 M will enhance the Li-ion mobility, thereby decreasing the magnitude of E_a .

2.4. Electrochemical study of G-SPE with LCMO

The electrochemical stability of the electrolyte G-SPE:1–3 M has been evaluated by combining it with an LCMO high-voltage cathode and Li metal anode in a coin-cell assembly at a current density of 20 mA g^{-1} within a potential range of 3–5.2 V (vs. Li). The GCD profile (Figure 5a,b) exhibits discharge capacities of 101, 104, and 108 mAh g^{-1} with capacity retention of 82, 79, and 63% after 100 cycles for G-SPE: 1, 2, and 3 M, respectively. The lowering in the capacity retention upon increasing the electrolyte concentration can be attributed to the increased number of F^- ions, which initiates parasitic side-reaction leading to electrolyte decomposition and material dissolution. The cyclic voltammetry (CV) profile of LCMO carried out at a scan rate of 0.1 mV s^{-1} has been depicted in Figure 5c. The CV exhibits oxidation and reduction peaks corresponding to $\text{Mn}^{4+}/\text{Mn}^{3+}$ and $\text{Co}^{3+}/\text{Co}^{2+}$ redox couples at 4.1 & 4.9 V vs. Li and 4.7 & 3.8 V vs. Li, respectively. The rate per-

formance study (Figure 5d) of the LCMO has been conducted in different G-SPE: 1–3 M at current density ranging from 20 to 100 mA g^{-1} . Similar to the GCD profile, the rate performance study illustrates an enhancement in the cycle stability and electrochemical performance of LCMO cycled in G-SPE:1 M and G-SPE:2 M, with a capacity retention of 71 and 77% after 50 cycles, while G-SPE:3 M shows a slight decrement in the electrochemical performance with a capacity retention of 61% after 50 cycles. Hence, the optimal concentration of the G-SPE is shown to be 1 and 2 M. Moreover, the GCD profile (Figure 5e,f) comparison of LCMO cycled in the liquid electrolyte (L.E.), and G-SPE further illustrates an enhancement in the cycle stability and capacity retention for the LCMO cycled in G-SPE to that cycled in L.E.

The EIS profile of the G-SPEs 1 to 3 M carried out at a frequency range of 10 kHz to 0.1 Hz has been shown in Figure 6a–f. The equivalent circuit (Figure 6g) of the EIS plots consists of solution-resistance (R_s), R_{CT-1} , and R_{CT-2} , which correspond to the resistance offered by the as-formed gel, and the SPE, Q is the constant phase element corresponds to the capacitive part, which shows the formation of a double layer, hence indicating the as-formed gel interface, at the high-frequency region, while the rising Warburg tail (Z_w) indicates the mass-transfer resistance at the low-frequency region.^[33] The Nyquist plot of LCMO cycled in G-SPE: 1 and 2 M shows an increase in the magnitude of R_{CT} in the initial cycles due to the formation of a gel interface that provides resistance to the Li-ion mobility. However, as the cycling progresses

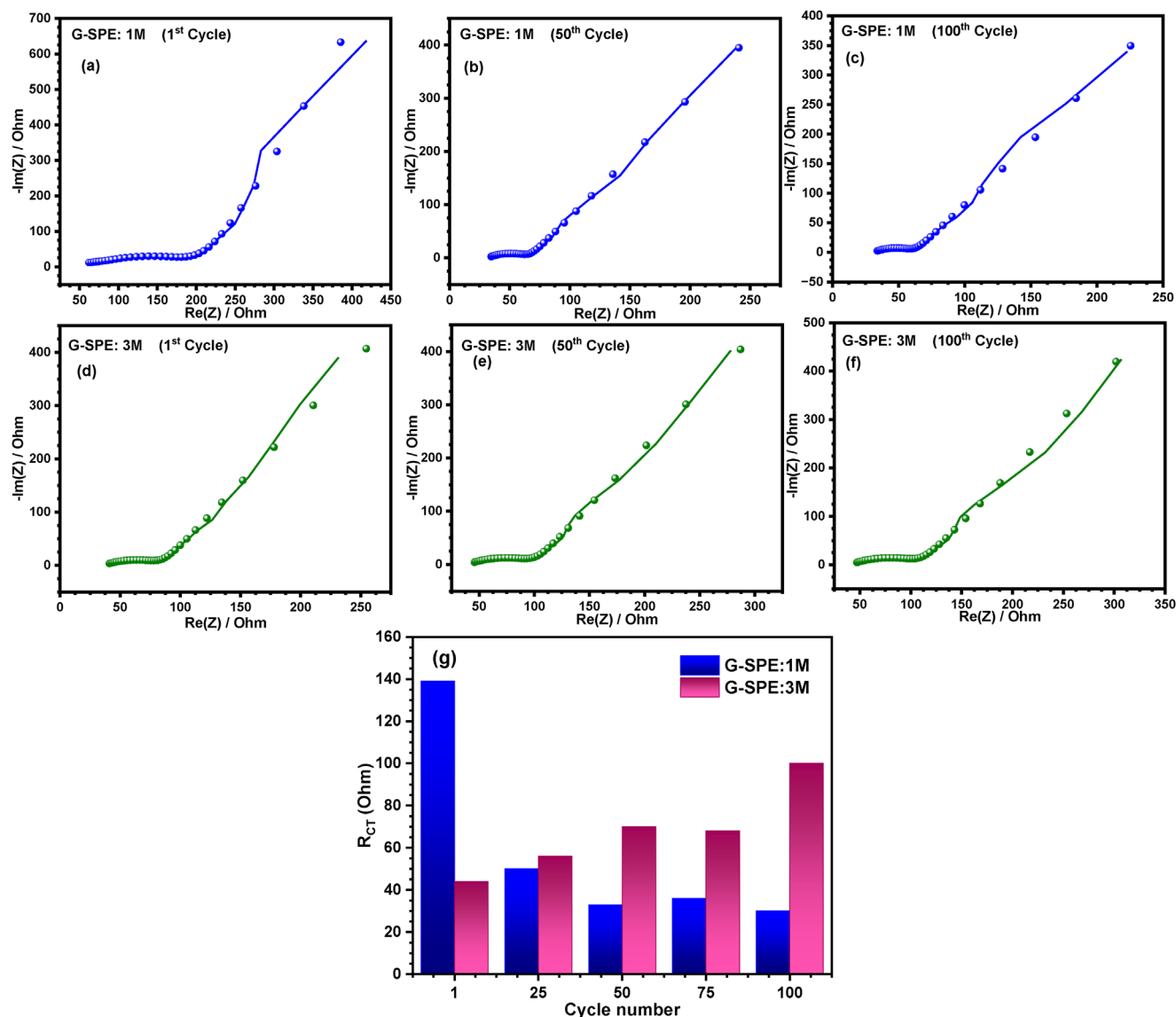


Figure 6. a–f) EIS plot and g) R_{CT} vs. cycle number plot of LCMO with G-SPE:1 m and G-SPE:3 m at different cycle numbers of 1st, 10th, 50th, and 100th cycle.

to the 50th and 100th cycles, the as-formed gel interface becomes stable such that no more increase in the R_{CT} can be observed. In contrast, a reverse of the trend can be observed for LCMO cycled in G-SPE: 3 m, wherein a rise in the magnitude of R_{CT} can be observed as the cycling progresses toward the 50th and 100th cycle, which can be attributed to the formation of an unstable gel-interface due to increasing number of F^- ions compared to G-SPE:1–2 m leading to parasitic side reactions and electrolyte decomposition, hence increasing the magnitude of R_{CT} and irreversibility.

To investigate the dynamic change in R_{CT} w.r.t the operating potential, an in-situ impedance analysis (Figure S8, Supporting Information) has been performed within the potential range of 3–5.2 V (vs. Li). The in-situ impedance plot of the first cycle exhibits a substantial increment in the magnitude of R_{CT} due to the conversion of liquid to gel electrolyte, which restricts the Li-ion

mobility. Also, R_{CT} exhibits an increase in its magnitude as the cycling progresses to high operating potentials. However, a decrease in the magnitude of R_{CT} can be observed as the cycling progresses to the tenth cycle. Also, compared to the first cycle, the tenth cycle exhibits a low and stable trend in the R_{CT} value as the cycling progresses to high operating potentials. Furthermore, the magnitude of R_{CT} eventually decreases as the cycle proceeds to the 50th cycle and then to the 100th cycle. These observations illustrate the stability of the as-formed gel interface, hence mitigating the irreversible capacity loss and improving the cycle stability.

The post-analysis of the G-SPEs and the electrodes was carried out using techniques such as XRD, XPS, and FE-SEM analysis. The XRD peaks of the uncycled G-SPE (Figure 7a) exhibit peaks at (100), (020) crystal plane, which shows the amorphous nature of the polymer matrix, and a less intense peak at (002)

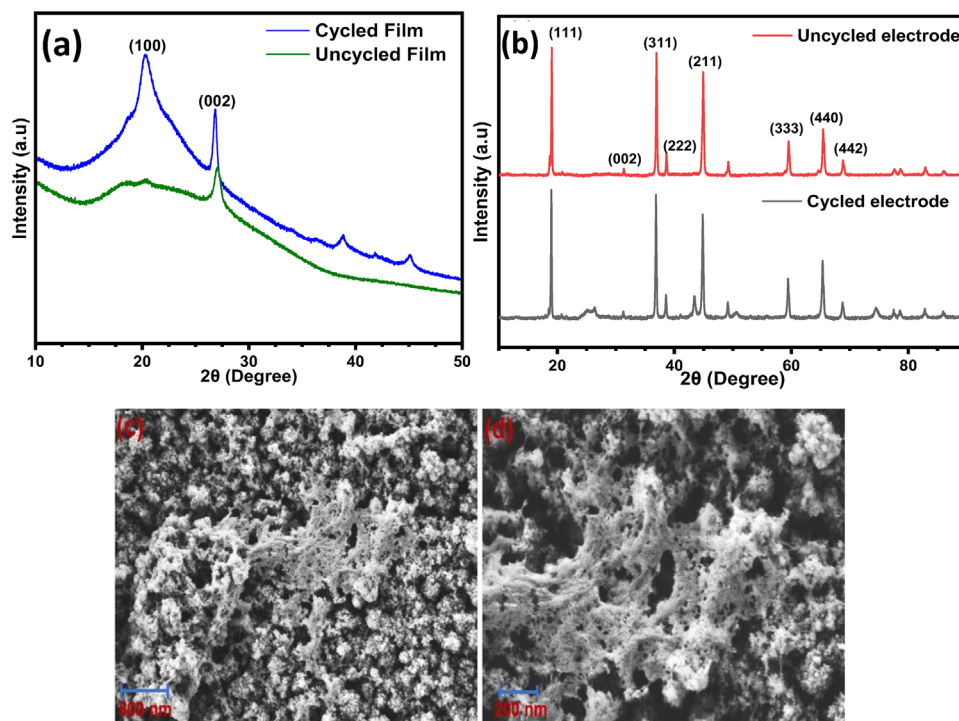


Figure 7. XRD spectra of cycled and uncycled a) LCMO electrode, b) G-SPE electrolyte, and c,d) FE-SEM image of cycled LCMO electrode.

corresponding to BN-filler in the film. However, in the cycled G-SPE, an intense peak has been observed at (100), showing a phase transition from amorphous to crystalline form due to the formation of the gel. In addition, the BN peak corresponding to the (002) crystal plane becomes more intense in the case of cycled G-SPE compared to the uncycled one. Further, the XRD spectra of the cycled LCMO electrode (Figure 7b) show characteristic peaks corresponding to (111), (311), and (211) crystal planes, which further reveals the absence of any phase change or structural distortion accompanying the charge–discharge. The XPS analysis of an intense peak of BN at (002) was observed for the cycled G-SPE compared to the uncycled G-SPE. Further, the XRD analysis of the cycled LCMO electrodes shows the characteristic peaks corresponding to (111), (311), and (211) crystal planes, which further reveals the absence of any phase change or structural distortion accompanying the charge–discharge. The FE-SEM analysis of the cycled LCMO electrodes is shown in Figure 7c,d. In addition, the EDS elemental analysis of the cycled and uncycled LCMO electrodes (Figure S9 and Table S4, Supporting Information) does not show any variation in the elemental distribution of Co and Mn in both electrodes, hence eliminating the occurrence of any transition metal dissolution. Further, the EDS analysis of cycled and uncycled G-SPE (Figure S10 and Table S5, Supporting Information) also shows similar properties with a uniform distribution of elements in both electrodes. Hence, these results are in complete agreement with the absence of any parasitic side reactions during cycling.

The XPS analysis of the cycled LCMO electrode and G-SPE: 3 M has been carried out to understand the occurrence of any parasitic side reactions or electrolyte decomposition accompanying the charge–discharge. The XPS spectra of the cycled LCMO

electrode (Figure S11, Supporting Information) show peaks corresponding to the P 2p, C 1s, O 1s, Mn 2p, F 1s, and Co 2p core levels. The deconvolution of the P 2p core level shows two peaks corresponding to LiPO_2F_2 (134 eV), which is the decomposed product of LiPF_6 hydrolysis, and the second corresponding to the un-decomposed LiPF_6 (137 eV) present in the electrolyte. In addition, the F 1s core level on deconvolution yields peaks corresponding to the decomposed products of LiF (685 eV) and LiPO_2F_2 (687 eV). The decomposition mechanism of LiPF_6 starts with the auto-ionization of LiPF_6 into LiF and PF_5 , followed by the hydrolysis of the PF_5 with a trace amount of water present in the electrolyte into POF_3 and HF. The HF will further react with POF_3 to form LiPO_2F_2 and $\text{Li}_2\text{PO}_3\text{F}$. All these products will form a major component of the SEI layer, while compared to the conventional liquid electrolytes, the phase transition of liquid into gel will mitigate further electrolyte decomposition, thereby enhancing the electrolyte stability and cell reversibility. In addition, the C1s core level on deconvolution shows peaks corresponding to O=C=O (287 eV), C–O–C (286 eV), and C–C (285 eV), wherein O=C=O, C–O–C, and C–C functionalities correspond to the PEC and SEI components of the gel-interface. In addition, similar to the C 1s core level, the O 1s core level on deconvolution yields peaks corresponding to functionalities of O=C=O (533 eV), C–O (532 eV), and C=O (531 eV). Also, the transition metal peaks corresponding to Mn 2p ($\text{Mn } 2p_{1/2}$ and $\text{Mn } 2p_{3/2}$) and Co 2p ($\text{Co } 2p_{1/2}$ and $\text{Co } 2p_{3/2}$) remain in the initial oxidation state of +4 and +3, which further illustrates the absence of any parasitic side-reactions leading to their dissolution. The XPS spectra of the G-SPE:3 M corresponding to P 2p, C 1s, O 1s, and F 1s core levels are shown in Figure S12 (Supporting Information). The P 2p core level on deconvolution yields peaks corresponding to the

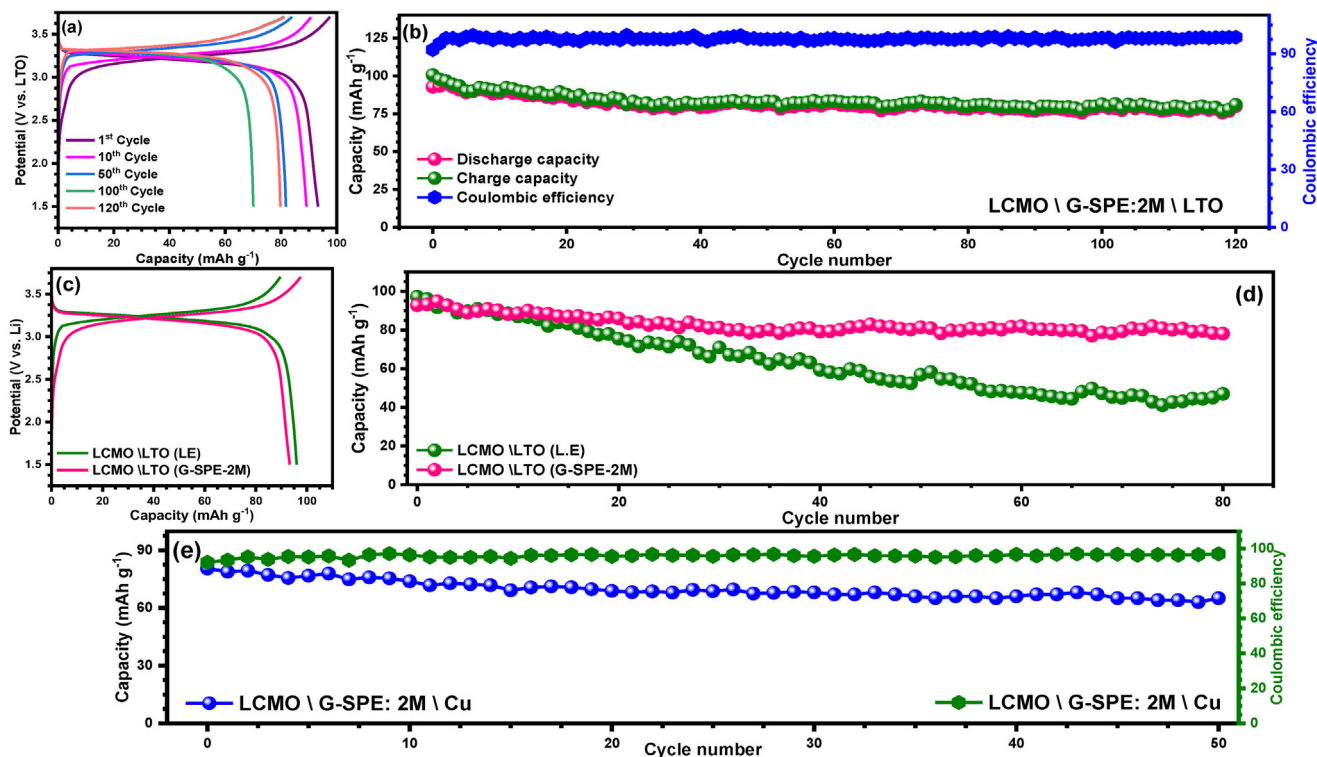


Figure 8. GCD profiles of a,b) LCMO\LTO cycled in G-SPE: 2 M, c,d) LCMO\LTO cycled in L.E and G-SPE: 2 M, e) LCMO\Cu cycled in G-SPE: 2 M.

SEI components, such as LiPO_2F_2 (134.2 eV) and Li_2POF_3 (136 eV), which is similar to that observed in the case of the LCMO electrode. The C 1s core level deconvolution shows peaks corresponding to the C—O—C (285.6), C—C (284.8 eV), and C=C (283 eV), which signifies the PEC component of the gel interface. Also, O 1s core-level on deconvolution shows peaks corresponding to C—O and C=O. The F 1s core-level on deconvolution exhibits different components of SEI, particularly Li_2POF_3 (683 eV) and LiF (685 eV). As already stated, the as-formed LiF-rich SEI layer by G-SPE:3 M will protect the surface of the LCMO electrode from parasitic side reactions. Hence, no transition metal can be observed either in bulk or at the interface of the G-SPE:3 M due to the absence of any transition metal dissolution.

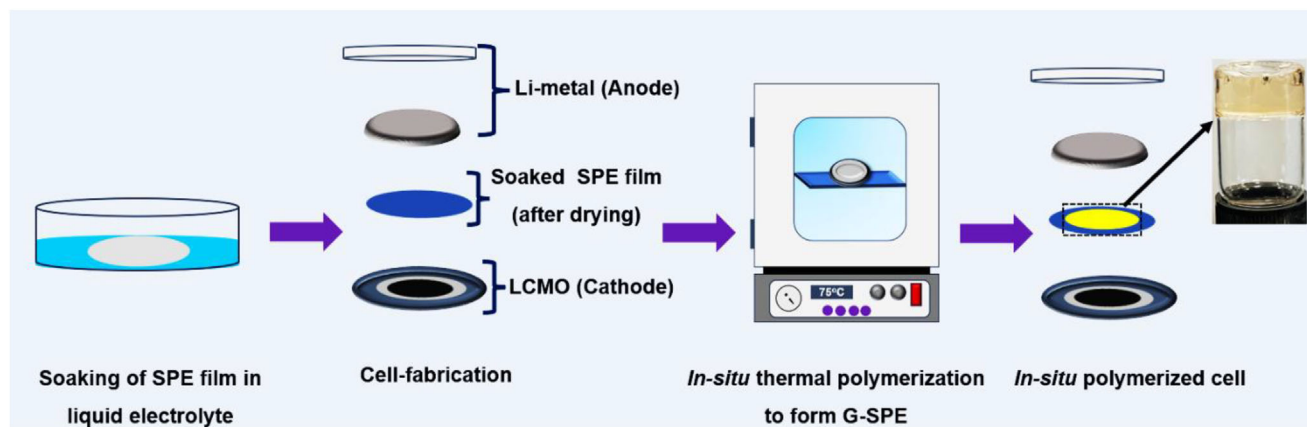
2.5. Full and Anode-Less Cell Study

The full-cell has been fabricated by coupling the LCMO against $\text{Li}_4\text{Ti}_5\text{O}_{12}$ (LTO) as anode using the optimized electrolyte combination of G-SPE:2 M, LCMO\G-SPE: 2 M\LTO, within the potential window of 1.5–3.7 V. The GCD plot of LCMO G-SPE: 2 M\LTO (Figure 8a,b) exhibits discharge capacities of 94 mAh g^{-1} with capacity retention of 86% and coulombic efficiency of 98% after 120 cycles. In addition, a comparison of the GCD profile of LCMO\LTO cycled in G-SPE:2 M and L.E (Figure 8c,d) further shows that the full-cell cycled in G-SPE:2 M exhibits superior electrochemical performance with capacity retention of 85% after 80 cycles, while the full-cell cycled in L.E shows capacity retention of 47% after 80 cycles. An anode-less cell has been fabricated by coupling the LCMO against a Cu strip using G-SPE: 2 M elec-

trolyte, LCMO\G-SPE: 2 M\Cu, and cycled within the potential range of 2.9–5.1 V (Figure 8e). The GCD profile of LCMO\G-SPE: 2 M\Cu exhibits excellent capacity retention of 82% and coulombic efficiency of 98% after 50 cycles. The excellent electrochemical performance of LCMO\LTO and LCMO\Cu in G-SPE:2 M can be attributed to the excellent interfacial stability of the as-formed gel, which mitigates electrolyte decomposition, thereby improving the cycle stability and eliminating the irreversible capacity loss.

3. Conclusion

Here, we successfully demonstrated the high-voltage stability of the solid electrolyte by combining the gel and solid polymer electrolyte, forming the so-called gel-solid polymer electrolyte or G-SPE. In addition, the nature of the as-formed gel has been analyzed by varying the electrolyte concentration from 1 to 3 M. The ionic conductivity of the G-SPEs, determined from the symmetric cell configuration of SS/G-SPE:1-3 M/SS, are in the order of $\approx 10^{-4} \text{ S cm}^{-1}$ with a higher magnitude for G-SPE:1 M due to the increase in the viscosity, which hinders the infiltration of electrolyte into the film. Moreover, the transference number also exhibited a similar result. In addition, the symmetric cell analysis of G-SPE:1-3 M electrolytes exhibits an enhancement in the stability for G-SPE:1-2 M, while polarisation occurs during the initial cycles for G-SPE:3 M, but it remains stable as the cycling progresses. The practical utility of the G-SPEs has been demonstrated by combining the G-SPE with an LCMO cathode and Li metal anode. The GCD profile exhibits better cycle stability and capacity retention for G-SPE:1-2 M, while a slight



Scheme 1. Typical *in-situ* polymerization process of G-SPE.

capacity degradation has been observed for G-SPE:3 m due to an increase in parasitic side reactions. Also, the cycled electrode and G-SPE post-analysis do not show any material dissolution or electrolyte degradation. Considering the present future, developing SPEs is a better way to improve the energy density of the LIBs, as the liquid electrolyte will decompose at high operating potentials. In addition, the research on SPEs has to be extended to the development of Ceramic, LISICON, and Argyrodite-based electrolytes for LIBs. In addition, research has to be extended to the development of novel polymers such as Polymethylmethacrylate (PMMA), Polyethylene oxide (PEO), and Polyacrylonitrile (PAN) for the development of SPEs.

4. Experimental Section

Preparation of the G-SPE: First, the SPE film was prepared using a solution casting method. Initially, 1 g of the polymer PVdF-HFP (Sigma-Aldrich, $M_w \approx 4,00,000$) was dissolved in a binary mixture of Acetone (Thermo Fischer) and tetrahydrofuran (1:1 by volume). To this mixture, 1.5 wt.% of BN was added and stirred overnight until the BN (Sigma-Aldrich, $\approx 1 \mu\text{m}$, 98%) was uniformly dispersed. The mixture was then cast onto a glass plate using a Doctor blade setup until a film was formed. The glass plate was kept aside for the solvent to evaporate, and the film was then cut into circular shapes using a separator cutter. The film was then kept overnight in a vacuum oven at 75 °C, until the moisture was removed. The film was taken into the glovebox with $\text{O}_2 < 0.1$ ppm and $\text{H}_2\text{O} < 0.1$ ppm. The film was then immersed in the liquid electrolyte so that the electrolyte could percolate into the film.

The liquid electrolyte was prepared inside an Ar-filled glovebox by dissolving different concentrations of LiPF_6 (Sigma-Aldrich, $\geq 99.99\%$) ranging from 1 to 3 m in a mixture of Ethylene carbonate (EC, Sigma-Aldrich) and Dimethylene carbonate (DMC, Sigma-Aldrich) in a 1:1 volume ratio, followed by the addition of the polymerization initiator Azobisisobutyronitrile (AIBN, Sigma-Aldrich). The as-prepared solution was stirred overnight until all the components were completely dissolved. The film was then immersed overnight in the liquid electrolyte for its percolation. The percolated film was then kept in a vacuum oven at 75 °C for the polymerization to occur, leading to the transformation of liquid electrolyte into gel; the as-formed combination of gel and SPE can be so-called gel-solid polymer electrolytes (G-SPE) (**Scheme 1**).

Synthesis and Electrode Preparation of LCMO Cathode: The LCMO was synthesized using a co-precipitation method. In the initial step, the stoichiometric amount of $\text{Co}(\text{CH}_3\text{COO})_2 \cdot 4\text{H}_2\text{O}$ (Sigma-Aldrich, $\geq 98\%$) and $\text{Mn}(\text{CH}_3\text{COO})_2 \cdot 4\text{H}_2\text{O}$ (Sigma-Aldrich, $\geq 99\%$) were dissolved in wa-

ter. Now, ethanol was added to the solution, followed by the addition of $(\text{NH}_4)_2\text{CO}_3$ (Sigma-Aldrich, $\geq 98\%$) to initiate the precipitation. The solution was kept aside for the precipitate to settle down. The precipitate was then washed with distilled water and ethanol, and then kept for drying. The dried sample was then calcined in air at 400 °C for 4 h. A stoichiometric amount of CH_3COOLi (Sigma-Aldrich, 99.95%) was mixed and subsequently subjected to calcination at 800 °C for 12 h.

Cell Fabrication: The electrode was prepared by mixing LCMO, conductive additive (Acetylene black), and binder (TAB-2, Teflonized acetylene black) in a weight ratio of 10:2:2 (in mg). The materials were evenly mixed using an ethanol medium until they became a circular and free-standing film. The as-obtained free-standing film was then fixed onto a stainless-steel mesh (14 mm, Goodfellow) using a hydraulic press (Specac, UK). The mass per unit area of the LCMO electrodes was within the range of 4–5 mg cm^{-2} . The electrode was kept overnight in a vacuum oven at 70 °C for the removal of moisture, if any. Now, the electrode was transferred into the glovebox, followed by the cell fabrication. The coin-cell (CR2016) fabrication was carried out in an Ar-filled glovebox with $\text{O}_2 < 0.1$ and $\text{H}_2\text{O} < 0.1$ ppm, in which the immersed SPE film will act as a separator as well as an electrolyte. The fabricated coin cells were kept inside a vacuum oven at 70 °C for 1 h for the polymerization of electrolytes, forming a gel interlayer between the electrode and the electrolyte^[34].

For the full cell, $\text{Li}_4\text{Ti}_5\text{O}_{12}$ (LTO) has been used as the anode. The LTO electrode was prepared by a solution casting method, where LTO, conductive additive (Acetylene black), and binder (PVDF) were mixed in a ratio of 80:10:10 in N-methylpyrrolidone (NMP, Sigma-Aldrich) as the solvent. The solution was stirred overnight until a thick slurry was obtained. The as-obtained slurry was cast on an aluminum foil using a doctor blade setup. The aluminum foil was kept for the solvent to evaporate, followed by cutting the electrode from the coated aluminum foil. The electrodes are kept in the vacuum oven to remove the moisture, followed by inserting it into an Ar-filled glove box. The LCMO was paired against LTO as an anode using a CR2016 coin-cell setup with G-SPE:2 m as electrolyte. The fabricated full-cell was kept inside a vacuum oven at 70 °C for 1 h for the polymerization of electrolytes, followed by testing the cell. For the anode-less cell, the LCMO electrode was paired against the Cu strip as a counter electrode.

The symmetric cell was fabricated with a configuration of $\text{Li}/\text{G-SPE}/\text{Li}$, which was used to evaluate the Li^+ transference number and stability of the electrolyte, whereas the stainless-steel (SS)/G-SPE/SS symmetric cells were used to determine the activation energy. In addition, the SS/G-SPE/SS symmetric cell was also used to determine the impedance characteristics of the electrolyte using electrochemical impedance spectroscopy (EIS), which was carried out within a frequency range of 1 kHz to 0.1 Hz with an applied a.c. amplitude of 10 mV. The asymmetric cells were fabricated with a configuration of SS/G-SPE/Li, which was used to perform the Linear-sweep voltammetry (LSV) of the electrolyte within a potential range of 3 to 7 V vs. Li. In addition, asymmetric cells were fabricated with LCMO

as cathode against Li anode with G-SPE: 1–3 m as the electrolyte, and the galvanostatic charge–discharge (GCD) cycling was conducted within a potential range of 3–5.2 V vs. Li. All the electrochemical studies were conducted in an electrochemical workstation (Solatron) and a battery tester (Biologic, France).

Material Characterization: The structure analysis of the electrodes and the polymeric film was studied by the X-ray diffraction analysis (XRD, Rigaku, Smart lab 9kW, monochromatic Cu K α radiation ($\lambda = 1.5406 \text{ \AA}$) with 2θ value ranging from 10 to 90° at a scan-rate of 0.2° min^{−1}. The infra-red spectral analysis of the G-SPE was carried out to understand the functional groups and components. The FE-SEM analysis (ZEISS, Gemini 560) was carried out to analyze the cross-section of the as-prepared film. In addition, the post-analysis was carried out for the G-SPE using both FE-SEM and XRD. The surface area and pore size of the polymeric film were determined using BET (Quantachrome) analysis. The electrolyte uptake by the polymeric film was quantified by immersing the polymeric film in the liquid electrolyte for 2 h. The amount of electrolyte percolated into the film has been quantified using the formula-

$$\% \text{electrolyte uptake} = (W_1 - W_2/W_2) \times 100 \quad (4)$$

where W_1 is the weight of the polymeric film after immersing it in the liquid electrolyte, and W_2 is the weight of the fresh polymeric film. The flammability of the G-SPE was tested by igniting the electrolyte with a lighter.

Theoretical Calculation: The theoretical calculations were carried out using the Gaussian 9 software. For the calculations, B3LYP functional was used with a 6–31G basis set.

Supporting Information

Supporting Information is available from the Wiley Online Library or from the author.

Acknowledgements

S.S. acknowledges the Council of Scientific and Industrial Research (CSIR) for the funding. Y.-S.L. acknowledges the financial support from the National Research Foundation of Korea (NRF) grant funded by the Korean government (Ministry of Science, ICT&Future Planning) (No. RS-2023-00208361). VA acknowledges financial support from the Anusandhan National Research Foundation (ANRF), Govt. of India, through Swarnajayanti Fellowship (SB/SJF/2020-21/12).

Conflict of Interest

The authors declare no conflict of interest.

Data Availability Statement

The data that support the findings of this study are available from the corresponding author upon reasonable request.

Keywords

coin-cell, high voltage cathode, ionic-conductivity, LiCoMnO₄, non-flammability, polymer electrolytes

Received: March 20, 2025
Revised: May 1, 2025
Published online: May 16, 2025

- [1] D. J. Wuebbles, A. K. Jain, *Fuel Process. Technol.* **2001**, 71, 99.
- [2] B. Smit, L. Ludlow, M. Brklacich, *J. Environ. Qual.* **1988**, 17, 519.
- [3] L. Al-Ghussain, *Environ. Prog. Sustain. Energy* **2019**, 38, 13.
- [4] H. Kondziella, T. Bruckner, *Renew. Sustain. Energy Rev.* **2016**, 53, 10.
- [5] M. Wang, G. Wang, Z. Sun, Y. Zhang, D. Xu, *Glob. Energy Interconnect.* **2019**, 2, 436.
- [6] S. Shafiee, E. Topal, *Appl. Energy* **2010**, 87, 988.
- [7] Y. Tian, G. Zeng, A. Rutt, T. Shi, H. Kim, J. Wang, J. Koettgen, Y. Sun, B. Ouyang, T. Chen, Z. Lun, Z. Rong, K. Persson, G. Ceder, *Chem. Rev.* **2021**, 121, 1623.
- [8] T. Kim, W. Song, D. Y. Son, L. K. Ono, Y. Qi, *J. Mater. Chem. A* **2019**, 7, 2942.
- [9] J. B. Goodenough, K. S. Park, *J. Am. Chem. Soc.* **2013**, 135, 1167.
- [10] J. B. Goodenough, Y. Kim, *Chem. Mater.* **2010**, 22, 587.
- [11] M. M. Thackeray, E. Lee, B. Shi, J. R. Croy, *J. Electrochem. Soc.* **2022**, 169, 20535..
- [12] S. Sreekumar, S. Natarajan, V. Aravindan, *Curr. Opin. Electrochem.* **2021**, 31, 100868.
- [13] A. Manthiram, *ACS Cent. Sci.* **2017**, 3, 1063.
- [14] X. Yu, W. A. Yu, A. Manthiram, *Small Methods* **2021**, 5, 2001196.
- [15] A. Manthiram, *Nat. Commun.* **2020**, 11, 1550.
- [16] W. Li, B. Song, A. Manthiram, *Chem. Soc. Rev.* **2017**, 46, 3006
- [17] J. Qian, L. Liu, J. Yang, S. Li, X. Wang, H. L. Zhuang, Y. Lu, *Nat. Commun.* **2018**, 9, 4918.
- [18] H. Xia, Z. Luo, J. Xie, *Prog. Nat. Sci. Mater. Int.* **2012**, 22, 572.
- [19] Y. Liu, X. Wu, K. Wang, Z. Feng, T. Cheng, Y. Liu, M. Wang, R. Chen, L. Xu, J. Zhou, Y. Lu, B. Guo, *Adv. Energy Mater.* **2021**, 11, 2000982.
- [20] F. I. Saaid, M. F. Kasim, T. Winie, K. A. Elong, A. Azahidi, N. D. Basri, M. K. Yaakob, M. S. Mastuli, S. N. Amira Shafiee, M. Z. Zolkiffly, M. R. Mahmood, *Heliyon* **2024**, 10, 23968.
- [21] T. Li, X. Z. Yuan, L. Zhang, D. Song, K. Shi, C. Bock, *Electrochem. Energy Rev.* **2020**, 3, 43.
- [22] M. Malik, K. H. Chan, G. Azimi, *Mater. Today Energy* **2022**, 28, 101066..
- [23] J. C. Barbosa, R. Gonçalves, C. M. Costa, S. Lanceros-Méndez, *ACS Omega* **2022**, 7, 14457.
- [24] Z. Zhang, R. G. Antonio, K. L. Choy, *J. Power Sources* **2019**, 435, 226736.
- [25] J. Castillo, A. Santiago, X. Judez, I. Garbayo, J. A. Coca Clemente, M. C. Morant-Miñana, A. Villaverde, J. A. González-Marcos, H. Zhang, M. Armand, C. Li, *Chem. Mater.* **2021**, 33, 8812.
- [26] J. Pan, P. Zhao, N. Wang, F. Huang, S. Dou, *Energy Environ. Sci.* **2022**, 15, 2753.
- [27] M. Liu, S. Zhang, G. Li, C. Wang, B. Li, M. Li, Y. Wang, H. Ming, Y. Wen, J. Qiu, J. Chen, P. Zhao, *J. Power Sources* **2021**, 484, 229235.
- [28] M. Yang, S. Li, G. Zhang, M. Huang, J. Duan, Y. Cui, B. Yue, H. Liu, *ACS Appl. Mater. Interfaces* **2023**, 15, 18323.
- [29] L. Chen, X. Fan, E. Hu, X. Ji, J. Chen, S. Hou, T. Deng, J. Li, D. Su, X. Yang, C. Wang, *Chem* **2019**, 5, 896.
- [30] S. Sreedeeep, Y. S. Lee, V. Aravindan, *Adv. Sustain. Syst.* **2023**, 7, 2300267.
- [31] S. Sreedeeep, Y. S. Lee, V. Aravindan, *Compos. Part B Eng.* **2024**, 277, 111365.
- [32] N. Reeves-McLaren, M. Hong, H. Alqurashi, L. Xue, J. Sharp, A. J. Rennie, R. Boston, *Energy Procedia* **2018**, 151, 158.
- [33] J. Wang, Y. Yamada, K. Sodeyama, C. H. Chiang, Y. Tateyama, A. Yamada, *Nat. Commun.* **2016**, 7, 1.
- [34] S. Sreedeeep, Y. Lee, V. Aravindan, *J. Mater. Chem. A* **2025**, 13, 13262.